

DRAFT VERSION JANUARY 5, 2026  
 Typeset using **LATEX modern** style in AASTeX7

## Betelgeuse: Detection of the Expanding Wake of the Companion Star

ANDREA K. DUPREE 

*Center for Astrophysics / Harvard & Smithsonian, 60 Garden St, Cambridge, MA 02138, United States*

PAUL I. CRISTOFARI \*

*Leiden Observatory, Leiden University, PO Box 9513, 2300 RA Leiden, The Netherlands*

MORGAN MACLEOD 

*Center for Astrophysics / Harvard & Smithsonian, 60 Garden St, Cambridge, MA 02138, United States*

KATERYNA KRAVCHENKO 

*Max Planck Institute for Extraterrestrial Physics, Gießenbachstraße 1, D-85748 Garching, Germany*

(Received 18 November 2025; Revised 13 December 2025; Accepted 16 December 2025)

Submitted to *Astrophysical Journal*

### ABSTRACT

Recent analyses conclude that Betelgeuse, a red supergiant star (HD 39801), likely has a companion object with a period of  $\sim 2000$  days orbiting at only  $2.3 R_\star$ , deep in the chromosphere of the supergiant. A probable detection of such a companion, named *Siwarha*, has just occurred from speckle imaging. This study finds that Betelgeuse spectra in the optical region and ultraviolet exhibit signatures of variable circumstellar absorption and chromospheric outflows. These variations are consistent with the  $\sim 2000$ -day period of the companion object. Circumstellar absorption evident in optical Mn I lines, and mass outflow marked by ultraviolet Fe II, Si I, and Mg I lines increase after the transit of the companion across the disk of Betelgeuse. Following the eclipse of the companion, the absorption and outflow slowly decrease in advance of the next transit. The occurrence and variation of this plasma appear consistent with the presence of a trailing and expanding wake caused by a companion star orbiting within the atmosphere of Betelgeuse.

**Keywords:** Stellar chromospheres (230), Stellar atmosphere (1584), Stellar mass loss (1613), M supergiant stars (988)

Corresponding author: A. K. Dupree

Email: [adupree@cfa.harvard.edu](mailto:adupree@cfa.harvard.edu), [cristofari@strw.leidenuniv.nl](mailto:cristofari@strw.leidenuniv.nl), [morgan.macleod@cfa.harvard.edu](mailto:morgan.macleod@cfa.harvard.edu), [kkravchenko@mpe.mpg.de](mailto:kkravchenko@mpe.mpg.de)

\* Center for Astrophysics | Harvard & Smithsonian, 60 Garden St, Cambridge, MA 02138, United States

## 1. INTRODUCTION

The red supergiant star, Betelgeuse (Alpha Orionis, HD 39801) has long been known to exhibit two periods of variation,  $\sim$ 400 days and  $\sim$ 2000 days, in apparent brightness, radial velocity, astrometric measures, and chromospheric emission lines (R. Stothers & K. Leung 1971; L. Goldberg 1984; E. Guinan 1984; A. Dupree et al. 1987; S. Ridgway 2013). While the 400-day period has been ascribed to the fundamental or low-overtone pulsational mode of the star (M. Joyce et al. 2020), the long secondary period (LSP) has been attributed to a number of causes: nonradial gravity modes, convective cells, binarity, dust formation or magnetic activity among them (L. Kiss et al. 2006; R. Stothers 2010; P. Wood et al. 2004; J. Percy & H. Sato 2009; I. Soszynski et al. 2021).

Two independent studies (J. Goldberg et al. 2024; M. MacLeod et al. 2025) conclude that the LSP is most likely caused by a companion star orbiting within the atmosphere of the supergiant. J. Goldberg et al. (2024) evaluated the many suggested explanations for the LSP and concluded that a companion star accompanied by a trailing cloud of dust could explain both the radial velocity and photometric variations. Similar clouds of dust had been invoked by I. Soszynski et al. (2021) to interpret the secondary periods observed in giant stars. M. MacLeod et al. (2025) assembled a century of measurements of radial velocity and visual magnitudes as well as astrometric measures to conclude also that Betelgeuse has a companion star. M. MacLeod et al. (2025) suggest the companion has a mass of  $0.6 \pm 0.14 M_{\odot}$ , and is orbiting at about  $2.3R_{\star}$  with its orbital plane perpendicular to the spin axis of the supergiant. The focus on binarity is also attractive because it offers an explanation for the observed fast rotation rate of Betelgeuse (H. Uitenbroek et al. 1998; P. Kervella et al. 2018).

Very recently, with speckle imaging techniques, a probable companion to Betelgeuse has been identified (S. Howell et al. 2025). Although the detection itself is not of high significance, the location and brightness of the companion are consistent with predictions which provide added weight to the feature in the speckle image. S. Howell et al. (2025) have named the companion *Siwarha* derived from the Arabic language to align with the origin of the name Betelgeuse. This name has just been adopted by the International Astronomical Union.<sup>5</sup>

The chromosphere of Betelgeuse, as signaled by Mg II emission, extends to a diameter of at least 270 mas (H. Uitenbroek et al. 1998) which corresponds to about  $6.4 R_{\star}$ , taking the observed infrared diameter at 42 mas (M. Montargès et al. 2014). Speckle imaging (S. Howell et al. 2025) in the optical region (466nm, 562nm) yields a similar diameter ( $41 \pm 1.2$  mas,  $40 \pm 1.4$  mas). Thus, the companion, orbiting at  $\sim 2.3R_{\star}$  lies within the stellar chromosphere. As M. MacLeod et al. (2025) noted, such a configu-

<sup>5</sup> See <https://exopla.net/star-names/modern-iau-star-names/>

ration could lead to a gravitationally focussed tail or wake following the companion. This paper seeks observational signatures of such a wake.

In the following sections, a brief summary of circumstellar lines in cool evolved stars (Section 2) is followed by measures of circumstellar Mn I transitions in Betelgeuse from optical spectra (Section 3). Ultraviolet lines indicative of mass outflow are discussed in Section 4 and Conclusions are summarized in Section 5.

## 2. CIRCUMSTELLAR LINES IN SUPERGIANT STARS

The search for circumstellar features originating in the spectra of supergiant stars began almost century ago when W. Adams and E. MacCormack (1935) noted asymmetry of several lines (Na D, Ca H and K) in the visible spectrum which were ascribed to circumstellar material. The advent of ultraviolet capability, first from balloon-borne spectrographs and subsequently the International Ultraviolet Explorer (IUE) produced many studies of circumstellar lines in luminous stars. The challenge of detecting cool circumstellar features against a cool photospheric spectrum was avoided by targeting a hot companion to the primary cool star. This companion provided a strong background continuum making it possible to detect a circumstellar absorption feature. Systems such as  $\alpha$  Scorpii (Antares), VV Cep, and AZ Cassiopeiae were good targets and produced many line identifications (K. van der Hucht et al. 1980; H.-J. Hagen et al. 1987; T. Kirsch & R. Baade 1994).

Betelgeuse presents a challenging object in which to discern circumstellar lines because it does not have a widely separated hot companion. However, R. Weymann (1962) in an extensive study of the Betelgeuse optical spectrum identified narrow circumstellar features from Fe I and Mn I as well as five doubly ionized species (Ca II, Sc II, Ti II, Si II, Ba II). Circumstellar lines also frequently appear against emission features arising from the chromosphere. Prominent among these are the Mg II emission lines near 2800Å which provide a variable background continuum to circumstellar Mn I and Fe I transitions located in the wings of Mg II. However, details of the circumstellar line width and its velocity are challenging to extract without a well-defined background emission line profile. Thus we focus here on optical circumstellar transitions.

Additionally the circumstellar envelope of Betelgeuse produces emission and this envelope has a diameter of 4 to 8 arcsec (A. Bernat & D. Lambert 1975), and extends possibly as far as 50 arcsec (R. Honeycutt et al. 1980). Thus a spectrum obtained with an aperture of  $\sim 4$  arcsec or larger will contain contaminating emission. Optical spectra suffer from this contamination, and emission from the circumstellar shell is frequently seen close by the absorption profile.

## 3. OPTICAL CIRCUMSTELLAR LINES IN BETELGEUSE

Optical spectra from two spectrographs are analysed here. HERMES is a high-resolution fibre-fed cross-dispersed echelle mounted on the 1.2m Mercator telescope

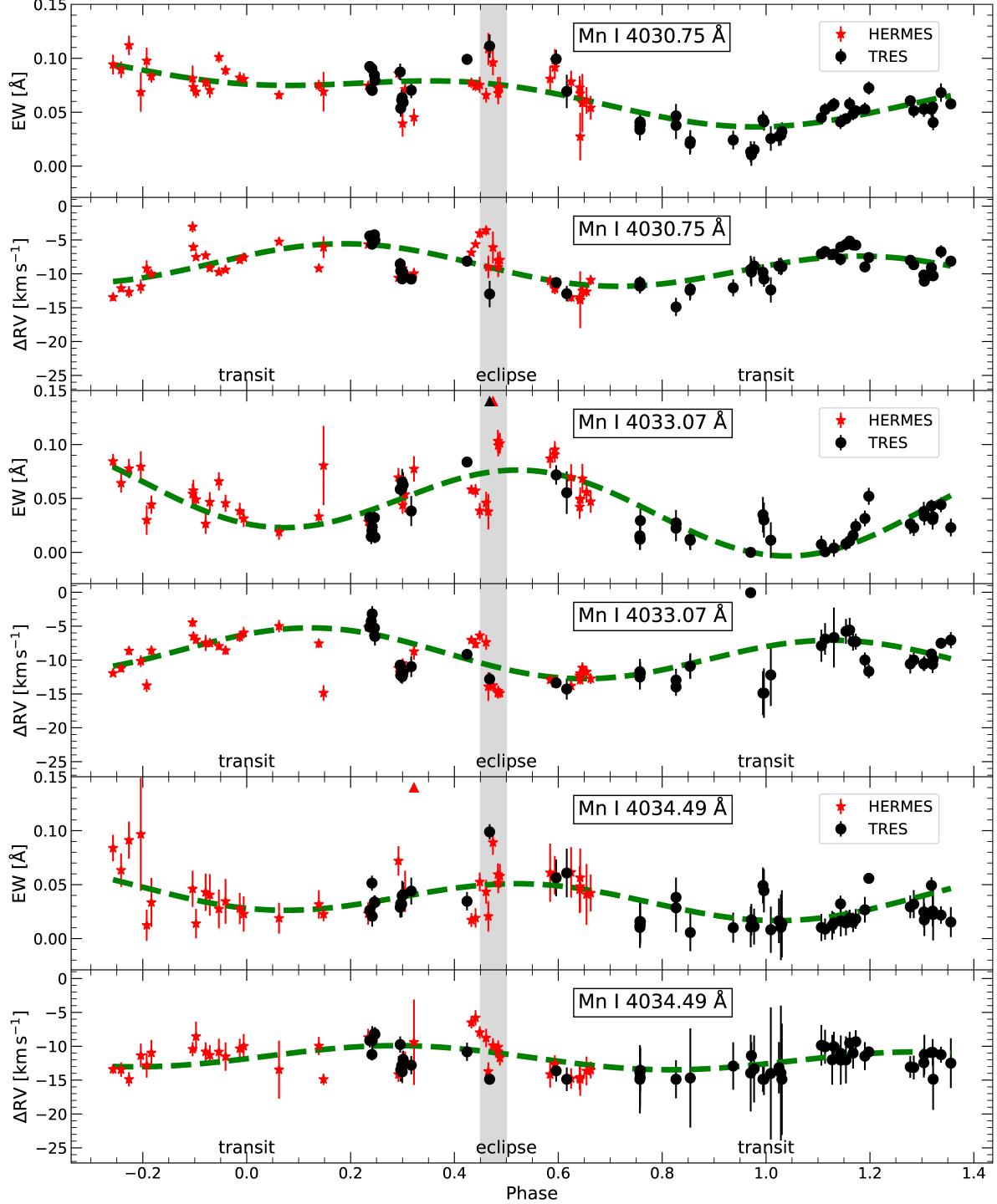


**Figure 1.** Measurements of three narrow circumstellar Mn I lines from the HERMES and TRES spectrographs. A 2-sine curve with a period of 2109 days is placed to guide the eye (broken green line). Filled red or black triangles mark a few outliers. *Upper panel for each line:* The equivalent width,  $EW(\text{\AA})$ , of the Mn I lines as a function of phase of the companion star. Phase 0 corresponds to the transit of the companion and phase 0.5 marks the eclipse of the companion. The negative phasing is used here for a few of the HERMES measures because they began prior to the TRES measures. *Lower panel for each line:* The relative radial velocity ( $\text{km s}^{-1}$ ) of the Mn I circumstellar line with respect to the photospheric line.

at the Roque de Los Muchachos Observatory, La Palma (Spain) with a spectral resolution of 86,000 and wavelength coverage from 3800Å to 9000Å (G. Raskin et al. 2011). About 43 HERMES spectra were obtained over a span of about 5.25 years: 2015 Nov 11 to 2021 May 2. Most of these spectra were included previously in a detailed tomographic analysis of the development of shock waves in the Betelgeuse photosphere prior to the Great Dimming (K. Kravchenko et al. 2021).

These spectra are complemented by spectra from TRES, which is a high-throughput cross-dispersed echelle spectrograph on the 1.5m Tillinghast telescope at FLWO Observatory at Mt. Hopkins, Arizona. TRES spectra cover 3900Å to 9100Å with a spectral resolution of 44,000. The 55 TRES spectra were obtained starting  $\sim$ 3 years after the start of HERMES spectra, from 2018 Sep 18 to 2025 Mar 04 - thus extending over  $\sim$ 6.5 years. The two overlap for about 2.7 years. Both sets of spectra offer good sampling of the 2109-day period, spanning almost two full epochs. Circumstellar transitions in Mn I also occur in the ultraviolet, most notably affecting the emission lines of Mg II (A. Lobel & A. Dupree 2000). However these ultraviolet transitions appear against the varying broad centrally-reversed line profiles of the strong Mg II emission near 2800Å, making extraction of line characteristics difficult.

In this analysis, the ephemeris of the companion is taken from M. MacLeod et al. (2025) as:  $T_0$  (transit, phase 0) = JD 2459988.29 corresponding to  $2023.12^{+0.34}_{-0.34}$ , and Period =  $2109 \pm 9$  days.

We focus on the Mn I triplet in the optical, which consists of 3 transitions (4030.75Å, 4033.07Å, and 4034.49Å) arising from the ground level of Mn I. To extract the line characteristics, a model of the spectrum is obtained by fitting two Gaussian profiles to the circumstellar and photospheric line. An interactive fitting procedure is adopted to obtain an optimal fit to both lines. First, a single Gaussian profile is fit to the broad photospheric line, and removed from the observed spectrum. This allows a first fit to the circumstellar line with another single Gaussian fit. To improve the fits, the modeled circumstellar line is removed from the original spectrum, and the process is repeated until the fitting parameters remain stable throughout iterations. This is shown schematically in Fig. 6 (Appendix). Five spectra are selected to display the 3 Mn I lines and the Gaussian fits at 5 phases of the companion’s orbit. These are shown in Fig. 7, 8, and 9 in the Appendix.

The equivalent width (EW) of the circumstellar line is extracted as well as the position of the line center relative to the center of the photospheric line. These values are shown in Fig 1 for each of the lines where the results from HERMES are shown with a negative phase, because some were obtained prior to the TRES observations.

Inspection of the changes in equivalent width of the narrow circumstellar line in the 3 Mn I transitions reveals a similar pattern among them. The minimum of the equivalent width occurs near transit of the companion (phase 0.0 and 1.0). The absorption continues to strengthen as the eclipse approaches (phase 0.5). After eclipse,

the equivalent width decreases. The HERMES spectra include observations before the start of the TRES spectra and so represent a different epoch. Changes in line strengths occur epoch to epoch, which is expected. Ultraviolet and infrared imaging have also shown changes in emission structures across the stellar surface on time scales of months (A. Dupree & R. Stefanik 2013; M. Montargès et al. 2016).

Another measurement of interest is the velocity shift of the circumstellar line with respect to the photospheric line. This shift as determined for each transition from the Gaussian fits to the line profiles is shown in the lower panel of Figure 1. An offset of  $\sim -5 \text{ km s}^{-1}$  from the photospheric velocity increases following the transit of the companion, reaching maximum outflow speed around eclipse,  $\sim -10$  to  $-15 \text{ km s}^{-1}$ , and then returns to a lower value. Such variations in expansion speed are characteristic of circumstellar material perhaps modulated by the presence of a companion object. Spiral structure outflows result from radiation hydrodynamic calculations of mass-losing binary star models (Z. Chen et al. 2020).

#### 4. ULTRAVIOLET CHROMOSPHERIC LINES IN BETELGEUSE

Ultraviolet line profiles are uniquely valuable in probing atmospheric dynamics. Many transitions, such as Fe II, Si I, and Mg I, with centrally reversed emission profiles, indicate mass motions in the chromosphere by their changing asymmetries. These changes have been modeled in detail to infer motion across the surface of Betelgeuse (A. Lobel & A. Dupree 2001).

The dynamics of the chromosphere are indicated by changes in relative strength of the line emission features. The ratio of the short-wavelength (“blue”) emission peak to the long-wavelength (“red”) emission peak in a centrally reversed profile characterizes the motion of the atmospheric material. The “blue” emission peak becomes weaker relative to the “red” peak when photons moving toward the observer encounter larger opacity on the blue side of the line (D. Hummer & G. Rybicki 1968). Such an asymmetry indicates outflowing material. Changes in line asymmetries and associated atmospheric velocity profiles have been calculated for Betelgeuse (A. Lobel & A. Dupree 2001) where it was demonstrated that increasing asymmetries in centrally reversed lines are caused by increasing velocities in the atmosphere. Thus, the asymmetry and its variation provide insight into the velocity field. In addition, details of the profiles, such as the shift and broadening of the central reversal also indicate mass motions at the highest regions of line formation in the atmosphere.

We now examine the behavior of seven ultraviolet chromospheric emission lines observed in Betelgeuse with HST/STIS spanning the years 2019 to 2025. This time interval of 2483 days exceeds the LSP of 2109 days.

Transitions from the ground state or low levels of Fe II at 2382.037Å, Mg I at 2852.1Å, and Si I at 2516.1Å are favorable to investigate the dynamics of the atmosphere. These strong lines exhibit emission with a central reversal that produces blue and red emission peaks. The central reversals are broad and deep - frequently with

**Table 1.** Selected Ultraviolet Transitions

| Species | Wavelength (Å) | E <sub>lower</sub> (eV) |
|---------|----------------|-------------------------|
| Si I    | 2516.112       | 0.03                    |
| Fe II   | 2585.876       | 0.0                     |
| Fe II   | 2692.834       | 0.99                    |
| Fe II   | 2724.883       | 1.04                    |
| Fe II   | 2727.538       | 1.04                    |
| Fe II   | 2730.734       | 1.08                    |
| Mg I    | 2852.127       | 0.0                     |

zero flux - making the detection of narrow circumstellar lines difficult, even if the spectral resolution is adequate. Wavelengths and energy levels for these ultraviolet lines are given in Table 1 and the changing relative line strengths are evaluated in the HST/STIS spectra in the following sections.

All of the 29 HST/STIS spectra used here were selected from the center pointings on Betelgeuse made with the  $0.025 \times 0.1$  arcsec aperture and the E230M grating (A. Dupree et al. 2020). They sample the center of the star which has a diameter of 42 mas in the infrared (M. Montargès et al. 2014) and a diameter of 125 mas in the continuum at 2500Å (R. Gilliland & A. Dupree 1996). However, the Mg II emission extends farther, exhibiting a diameter of 270 mas, corresponding to a radius  $6.4 R_{\star}$  (H. Uitenbroek et al. 1998). The emission from a circumstellar envelope is not present in the HST spectra we use, because the small spectroscopic aperture ( $0.025 \times 0.100$  arcsec) offered by HST/STIS avoids the emission contributions from the circumstellar envelope (A. Bernat & D. Lambert 1975) which has a diameter of 4 to 8 arcsec. The spectra used and line ratios are given in Appendix/Table 2, and discussed individually in the following sections.

#### 4.1. Fe II 2692.83Å

**Three** HST/STIS spectra at 2692Å taken at the Betelgeuse center at different phases are displayed in Figure 2 (*top left panel*). These spectra were selected from those listed in Table 2. We take the ratio of the maximum flux in the short-wavelength emission feature to that in the long wavelength emission feature (blue/red) as the parameter of choice to assess the presence of asymmetries. The decrease in total line flux from phase 0.03 to 0.50 is caused by the weakening of the "blue" emission.

This ratio shown in Fig. 2 (*top right panel*) decreases post-transit, indicating that increased chromospheric outflow is present from phase 0.0 (transit) to  $\sim 0.7$  (post-eclipse). The outflow reaches a maximum value following eclipse of the companion. Subsequent reduction of the outflow velocity returns the chromosphere to its previous

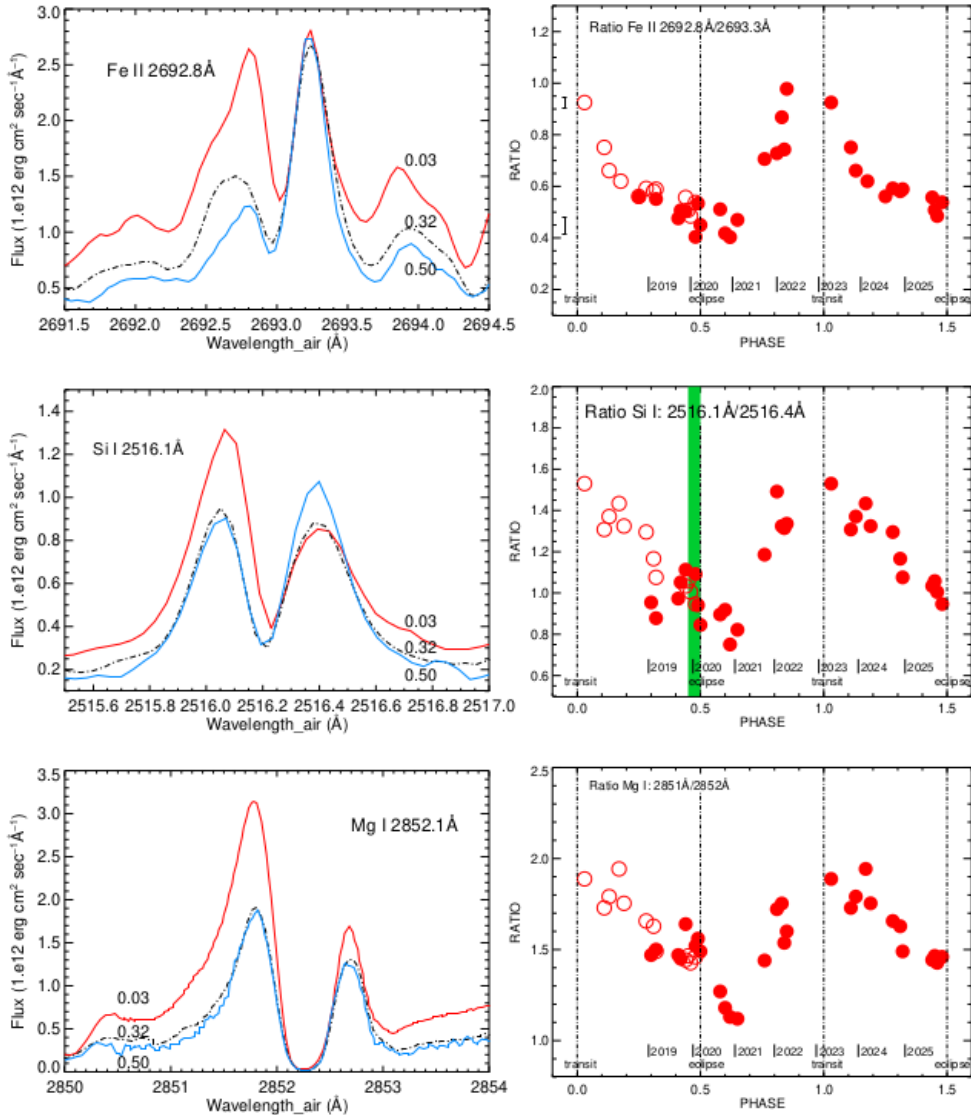


**Figure 2.** *Left panel:* Chromospheric transitions (Fe II, Si I, Mg I) at three phases. The time sequence has been inverted for display. Spectra at phases 0.03 and 0.32 were obtained in 2023 and 2024 respectively; the spectrum at phase 0.50 was obtained in 2020. The central absorption extending toward shorter wavelengths marks the expanding chromosphere after transit of the companion (phase 0). The decrease in total line flux is caused by the substantial weakening of the short wavelength emission. *Right panel:* The ratio of the peaks, (blue/red), as a function of phase of the binary. Phases 1.0 to 1.4 (2023-2025) are repeated in the figure at phase 0.0 to 0.4 and marked by open circles. The green band in the middle panel marks the Great Dimming: 2019 December- 2020 February.

state, marking the  $\sim 2000$  day period. Three of the ultraviolet observations were made during the passage of plasma from the Surface Mass Ejection in 2019 Sep.-Nov. (phase 0.41-0.44) prior to the Great Dimming in 2020 Feb. However, that ejection appeared to occur principally in the south to south east quadrant of the star (M. Montargès et al. 2021; A. Dupree et al. 2020, 2022) and the ratios of these transitions do not appear

discrepant from the others. Moreover, as this and subsequent spectra demonstrate, the pattern is similar during 2025 when a Great Dimming event has not occurred.

The shape of the central reversal can also indicate chromospheric motions at the highest levels of line formation. In Fig 2 (*left panels*), the reversal has a shift of the short wavelength wing post-transit in agreement with the inference from the line emission ratios. The greater short wavelength extent ( $\sim 0.18\text{\AA}$ ) of the central absorption at phase  $\sim 0.5$ , an indicator of mass outflow, corresponds to  $\sim -20\text{ km s}^{-1}$ . This value is somewhat larger than the values indicated by the distant circumstellar features, but not surprising as the Betelgeuse wind does not appear to be similar to the solar wind that accelerates to supersonic velocities (S. Cranmer & A. Winebarger 2019).

#### 4.2. $\text{Si I } 2516.1\text{\AA}$

This transition arises from a low lying level (0.03 eV) of Si I, and the mass motions also affect the short-wavelength emission of the transition (Fig. 2, middle panel). This transition was evaluated in detail at various positions on the Betelgeuse disk which demonstrated the impact of a changing velocity field on the line asymmetries (A. Lobel & A. Dupree 2001). We construct the ratio of the flux of the blue emission peak to that of the red emission peak:  $2516.1\text{\AA}/2516.4\text{\AA}$ . This blue/red ratio shows a variation similar to that of the Fe II line discussed previously. Moreover as shown in the left panel of Fig. 2, the centrally reversed profile is broadened towards shorter wavelengths by  $\sim 0.06\text{\AA}$ , in the spectra taken at phase 0.32 and 0.50. This shift amounts to  $\sim -7\text{ km s}^{-1}$ .

cd

#### 4.3. $\text{Mg I } 2852.1\text{\AA}$

The transition from the ground state of Mg I is also a likely candidate to track the circumstellar material. However the broad central reversal spanning  $\sim 0.2\text{\AA}$  or  $\sim 21\text{ km s}^{-1}$  with essentially zero flux, prevents a clear detection of a circumstellar transition. A slight weakening appears on the short wavelength side of the centrally reversed chromospheric profile (Fig. 2, lower panel). The ratio of the short wavelength:long wavelength peak tracks the changing absorption in the outflowing chromosphere similar to that in Si I and Fe II.

#### 4.4. Additional Fe II lines

To ensure that the 3 transitions of Si I, Mg I and Fe II were not anomalous, we evaluate 4 additional lines ranging in excitation potential from 0 to 1.08 eV. Line profiles at 3 phases are shown in Fig. 3 where a short wavelength expansion of the central reversal post-transit is visible and amounts to  $\sim -9$  to  $-12\text{ km s}^{-1}$ . The blue/red ratios for these transitions are shown in Figure 4. The pattern of increased outflow post-transit is found in all lines and replicates those discussed previously.

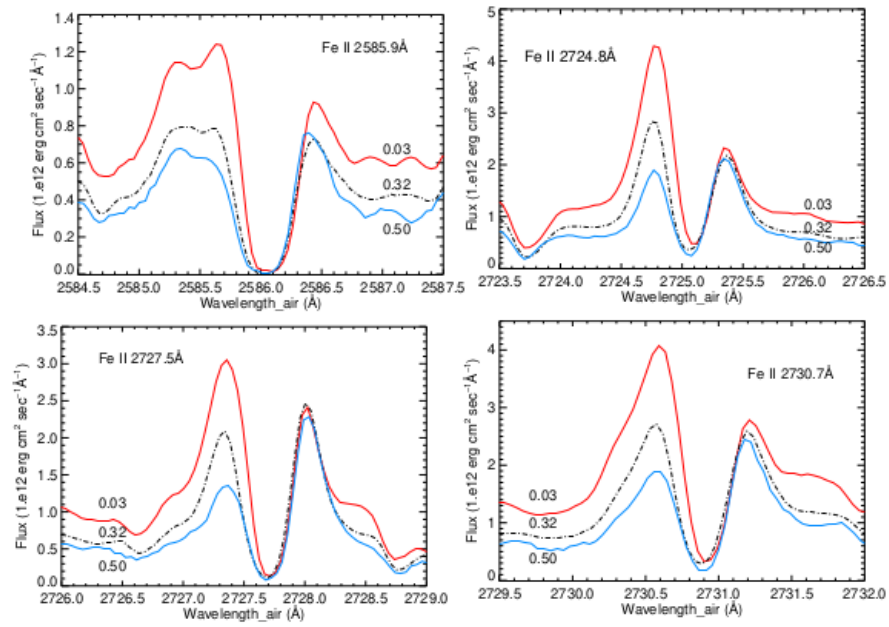


**Figure 3.** Four Fe II transitions at three phases of the LSP. The time sequence has been inverted for display as in Fig. 2. Absorption extending toward shorter wavelengths indicates the expanding chromosphere after transit of the companion (phase 0). The asymmetry of the profiles changes with phase, displaying the weakening in the blue emission produced by the opacity in the expanding atmosphere and signaled by a decrease in the blue/red ratios.

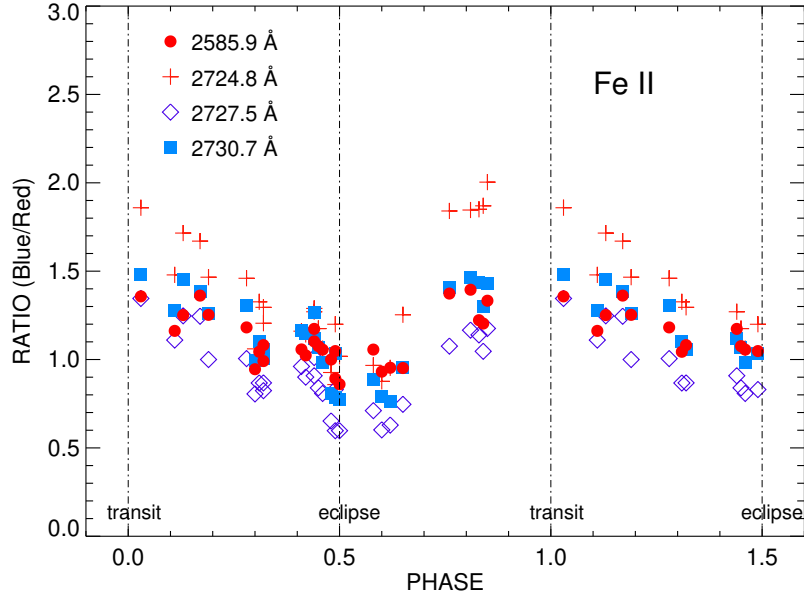


**Figure 4.** The asymmetry ratio (blue/red) for four Fe II transitions whose profiles are shown in Fig. 3.

## 5. CONCLUSIONS

The EW changes in the optical circumstellar Mn I lines demonstrate variability consistent with the LSP. Adopting the model that a companion object causes the LSP variation, we find that the phasing indicates that circumstellar absorption increases immediately following the transit of the companion across the disk of Betelgeuse (phase 0.0), reaching a maximum at about phase 0.5 and then begins to decrease, returning to its initial state after  $\sim 2100$  days. This pattern is similar to the optical (V) variation found in the LSP of Betelgeuse, namely brightest at phase 0 and faintest at phase 0.5 (M. MacLeod et al. 2025). Thus it appears possible that the variation of the circumstellar material contributes to the optical variation.

In addition, the circumstellar lines display a variation in expansion velocity relative to the photosphere, consistent with the LSP. As Fig. 1 shows, following transit (phase 0.0) the circumstellar outflow from the photosphere begins, reaching a maximum value of  $\sim -5$  to  $-10$  km s $^{-1}$  near phase  $\sim 0.7$ .

The asymmetry changes in the ultraviolet emission line profiles signal that outflow of the chromosphere also begins post-transit and continues through eclipse. The chromospheric expansion is present until phase  $\sim 0.7$  when it decreases rapidly as transit approaches, signaling a weakening of the outflowing motion. This velocity variation has a period approximately equal to the LSP, and it is asymmetric, reaching a maximum outflow at phase  $\sim 0.7$  followed by a rapid recovery as transit approaches. The broadened shift of the central reversal of the chromospheric lines ranges from  $-6$  to  $-20$  km s $^{-1}$ , values commensurate with the circumstellar features. Thus the chromosphere and the circumstellar material appear to move in similar fashion over the LSP.

If the postulated and probably-detected companion to Betelgeuse is confirmed (J. Goldberg et al. 2024; M. MacLeod et al. 2025; S. Howell et al. 2025), we might understand the spectroscopic variations described here as follows. A companion orbiting in a  $\sim 6$  year period around Betelgeuse moves at an orbital velocity of  $\sim 43$  km s $^{-1}$  (M. MacLeod et al. 2025). The chromosphere region of Betelgeuse is a mixed environment of multi-phase gas ranging from several to ten thousand Kelvin in temperature. At a representative  $\sim 2500$ K temperature for the intermediate temperature gas (E. O’Gorman et al. 2020), the sound speed is  $\sim 6$  km s $^{-1}$  and the motion of the companion has a relative Mach number through the stellar wind of  $\mathcal{M} \sim 7$ . In the chromosphere, the expansion velocity of the wind is similar to that of the circumstellar absorption, on the order of 10 km s $^{-1}$  while the turbulent velocity is even higher,  $\sim 20$  km s $^{-1}$  (A. Lobel & A. Dupree 2001; N. Soker 2021; S. Fuller & D. Tsuna 2024; J-Z. Ma et al. 2025). The companion would gravitationally focus surrounding wind into its vicinity, forming a trailing wake, whose primary orientation would be along the direction of the orbital path (Z. Chen et al. 2020, see Figure 5). Within this wake, denser, shocked gas would be swept up and accumulate behind the passing shockwave

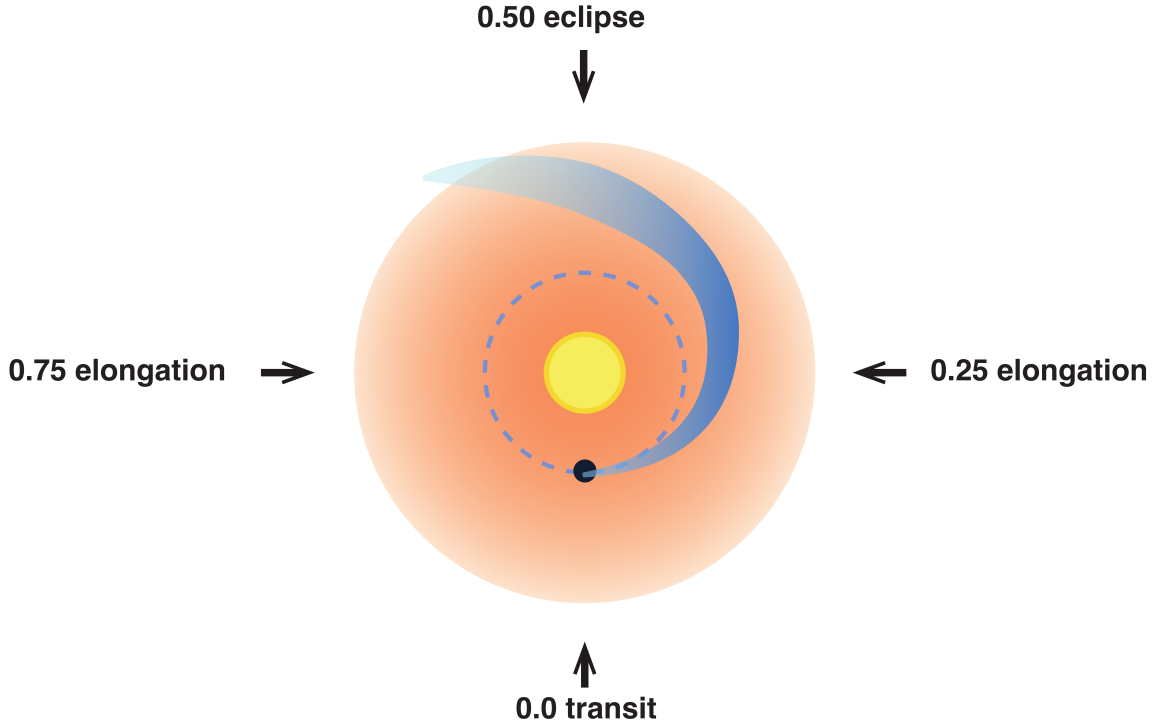


**Figure 5.** A schematic drawing from above of Betelgeuse and the observed wake caused by the companion star. The orbit of the companion, at  $\sim 2.3 R_{\star}$  is shown by a broken blue line. It is well within the total extent of the Mg II emission which reaches  $6.4 R_{\star}$  - marked by diffuse orange color. When observed at different phases, along the direction of the arrows, the expanding wake can be detected.

(Credit: A.H. Szentgyorgyi)

(E. Ostriker 1999). We should expect this wake to be quite variable because of the multi-temperature turbulent gas it exists in, and because the turbulent velocity is larger than the mean sound-speed and a large fraction of the orbital speed.

Lines of sight passing through the wake would pass through denser, shocked material. The wake expands laterally at the sound speed,  $\sim 6 \text{ km s}^{-1}$ . Thus while it is small during transit of the companion across Betelgeuse's disk, it widens and covers a larger fraction of the disk as the orbit progresses. The estimated time to cover Betelgeuse's radius is  $\sim 800 R_{\odot} / 6 \text{ km s}^{-1} \approx 3 \text{ yr}$ . During this time, the companion has completed a half-orbit from transit to the vicinity of eclipse. Compared to our observational data, a half-orbit offset from transit (i.e. eclipse at phase 0.5) is the time of minimum optical brightness in the LSP and comparable to the most significant excess chromospheric absorption of both optical and UV lines in these current observations. As the orbit progresses further, the wake still exists, but as it widens, its effect is diluted by its continued expansion (E. Ostriker 1999). Clearly, more sophisticated modeling, perhaps capturing the thermodynamic properties of the

chromosphere region (e.g. B. Freytag & S. Höfner 2008; S. Wedemeyer et al. 2017; J-Z. Ma et al. 2025) along with the effect of an orbiting companion (e.g. Z. Chen et al. 2020), is eventually needed. In particular, the shock heating and radiative cooling and the confluence of the gravitationally-focused wake will determine the wake density contrast, along with its characteristic temperature. These factors are crucial to predicting the emergent spectra and are best modeled in a hydrodynamic context.

These results add direct spectroscopic evidence that the extended atmosphere of Betelgeuse is modulated on timescales associated with the LSP. This evidence supports the hypothesis of the presence of a companion object in the atmosphere of Betelgeuse. In particular, the fact that the photosphere, the chromosphere, and circumstellar lines all appear to vary in intensity and radial velocity in synchronization with this long period does appear to be best explained by a companion star orbiting within the extended atmosphere. We suggest that a trailing wake geometry is most consistent with the observations, and calculations of the wake structure and the emergence of spectral lines from it are needed. Because the companion is separated by only  $\sim 2.3 R_*$ , it is obscured by the large Betelgeuse disk at the current phase  $\sim 0.5$ , and will be visible again at phase  $\sim 0.6$  which occurs in August 2027.

## 6. DATA AVAILABILITY

Most of the HERMES spectra are published in K. Kravchenko et al.(2021) and are available at the CDS via anonymous ftp to cdsarc.u-strasbg.fr (<ftp://130.79.128.5>) or via <http://cdsarc.u-strasbg.fr/viz-bin/cat/J/A+A/650/L17>. The HST data described here may be obtained from the MAST archive at [doi: 10.17909/zz3e-gh10](https://doi.org/10.17909/zz3e-gh10). Remaining spectra from HERMES and those of TRES are available from the authors.

*Facilities:* HST(STIS), 1.2m Mercator telescope (HERMES), FLWO(TRES)

*Software:* astropy, IDL, IRAF, Adobe Photoshop

## ACKNOWLEDGEMENTS

We are grateful to the referee whose suggestions improved the presentations found here. Based on observations made with the Mercator Telescope, operated on the island of La Palma by the Flemish Community, at the Spanish Observatorio del Roque de los Muchachos of the Instituto de Astrofísica de Canarias. These spectra were obtained with the HERMES spectrograph, which is supported by the Research Foundation - Flanders (FWO), Belgium, the Research Council of KU Leuven, Belgium, the Fonds National de la Recherche Scientifique (F.R.S.-FNRS), Belgium, the Royal Observatory of Belgium, the Observatoire de Genève, Switzerland and the Thüringer Landessternwarte Tautenburg, Germany. This research is also based on ultraviolet observations made with the NASA/ESA Hubble Space Telescope obtained from the Space Telescope Science Institute, which is operated by the Association of Universities

for Research in Astronomy, Inc., under NASA contract NAS 5-26555. These observations are associated with programs GO 15641, 15873, 16216, 16655, 16984, 17522, and 17845. This work was supported in part by STScI Grant HST-GO-15641.001-A to the Smithsonian Astrophysical Observatory.

## AUTHOR CONTRIBUTIONS

HST/STIS and TRES spectra were obtained by A. Dupree; K. Kravchenko obtained the HERMES spectra; P. Cristofari and A. Dupree analyzed the spectra. M. MacLeod contributed to the theoretical interpretation. All of the authors contributed to the discussion and conclusion.

## REFERENCES

Adams, W. S. & MacCormack, E. 1935, *ApJ*, 81, 119. doi:10.1086/143620

Bernat, A. P. & Lambert, D. L. 1975, *ApJL*, 201, L153. doi:10.1086/181964

Chen, Z., Ivanova, N., & Carroll-Nellenback, J. 2020, *ApJ*, 892, 110. doi: 10.3847/1538-4357/ab7b6e

Cranmer, S. R. & Winebarger, A. R. 2019, *ARA&A*, 57, 157. doi:10.1146/annurev-astro-091918-104416

Dupree, A. K., Baliunas, S. L., Guinan, E. F., et al. 1987, *ApJL*, 317, L85. doi:10.1086/184917

Dupree, A. K. & Stefanik, R. P. 2013, *EAS Pub. Series*, 60, 77. doi:10.1051/eas/1360008

Dupree, A. K., Strassmeier, K. G., Matthews, L. D., et al. 2020, *ApJ*, 899, 68. doi:10.3847/1538-4357/aba516

Dupree, A. K., Strassmeier, K. G., Calderwood, T., et al. 2022, *ApJ*, 936, 18. doi:10.3847/1538-4357/ac7853

Freytag, B. & Höfner, S. 2008, *A&A*, 483, 571. doi:10.1051/0004-6361:20078096

Fuller, J. & Tsuna, D. 2024, *The Open Journal of Astrophysics*, 7, 47. doi:10.33232/001c.120130

Gilliland, R. L. & Dupree, A. K. 1996, *ApJL*, 463, L29. doi:10.1086/310043

Goldberg, J. A., Joyce, M., & Molnár, L. 2024, *ApJ*, 977, 35. doi:10.3847/1538-4357/ad87f4

Goldberg, L. 1984, *PASP*, 96, 366. doi:10.1086/131347

Guinan, E. F. 1984, *Cool Stars, Stellar Systems, and the Sun*, 193, 336. doi:10.1007/3-540-12907-3\_225

Hagen, H.-J., Hempe, K., & Reimers, D. 1987, *A&A*, 184, 256.

Honeycutt, R. K., Kephart, J. E., Bernat, A. P., et al. 1980, *ApJ*, 239, 565. doi:10.1086/158142

Howell, S. B., Ciardi, D. R., Clark, C. A., et al. 2025, *ApJL*, 988L, 47H. doi:10.3847/2041-821

Hummer, D. G. & Rybicki, G. B. 1968, *ApJL*, 153, L107. doi:10.1086/180231

Joyce, M., Leung, S.-C., Molnár, L., et al. 2020, *ApJ*, 902, 1, 63. doi:10.3847/1538-4357/abb8db

Kervella, P., Decin, L., Richards, A. M. S. et al. 2018, *A&A*, 609, A67. doi:10.1051/0004-6361/201731761

Kirsch, T. & Baade, R. 1994, *A&A*, 291, 535.

Kiss, L. L., Szabó, G. M., & Bedding, T. R. 2006, *MNRAS*, 372, 1721. doi:10.1111/j.1365-2966.2006.10973.x

Kravchenko, K., Jorissen, A., VanEck, S. et al. 2021, *A&A*, 650, L17. doi:10.1051/0004-6361/202039801

Lobel, A. & Dupree, A. K. 2000, *ApJ*, 545, 454. doi: 10.1086/317784

Lobel, A. & Dupree, A. K. 2001, *ApJ*, 558, 815. doi:10.1086/322284

Ma, J-Z., Justham, S., Pakmor, R. et al. 2025, eprint arXiv:2510.14875. doi:10.48550/arXiv.2510.14875

MacLeod, M., Blunt, S., De Rosa, R. J., et al. 2025, *ApJ*, 978, 50.  
doi:10.3847/1538-4357/ad93c8

Montargès, M., Kervella, P., Perrin, G., et al. 2014, *A&A*, 572, A17.  
doi:10.1051/0004-6361/201423538

Montargès, M., Kervella, P., Perrin, G., et al. 2016, *A&A*, 588, A130.  
doi:10.1051/0004-6361/201527028

Montargès, M., Cannon, E., Lagadec, E., et al. 2021, *Nature*, 594, 7863, 365.  
doi:10.1038/s41586-021-03546-8

O’Gorman, E., Harper, G. M., Ohnaka, K. et al. 2020, *A&A*, 638, A65.  
doi:10.1051/0004-6361/202037756

Ostriker, E. C. 1999, *ApJ*, 513, 1, 252.  
doi:10.1086/306858

Percy, J. R. & Sato, H. 2009, *JRASC*, 103, 1, 11.

Raskin, G., van Winckel, H., Hensberge, H., et al. 2011, *A&A*, 526, A69.  
doi:10.1051/0004-6361/201015435

Ridgway, S. T. 2013, *EAS Publications Series*, 60, 5. doi:10.1051/eas/1360001

Soker, N. 2021, *ApJ*, 906, 1, 1.  
doi:10.3847/1538-4357/abca8

Soszyński, I., Olechowska, A., Ratajczak, M., et al. 2021, *ApJL*, 911, L22.  
doi:10.3847/2041-8213/abf3c9

Stothers, R. B. 2010, *ApJ*, 725, 1, 1170.  
doi:10.1088/0004-637X/725/1/1170

Stothers, R. & Leung, K. C. 1971, *A&A*, 10, 290

Uitenbroek, H., Dupree, A. K., & Gilliland, R. L. 1998, *AJ*, 116, 5, 2501.  
doi:10.1086/300596

van der Hucht, K. A., Bernat, A. P., & Kondo, Y. 1980, *A&A*, 82, 14.

Wedemeyer, S., Kučinskas, A., Klevas, J., & Ludwig, H-G. 2017, *A&A*, 606 A26:  
doi:10.1051/0004-6361/201730405

Weymann, R. 1962, *ApJ*, 136, 844.  
doi:10.1086/147441

Wood, P. R., Olivier, E. A., & Kawaler, S. D. 2004, *ApJ*, 604, 800.  
doi:10.1086/382123

## APPENDIX

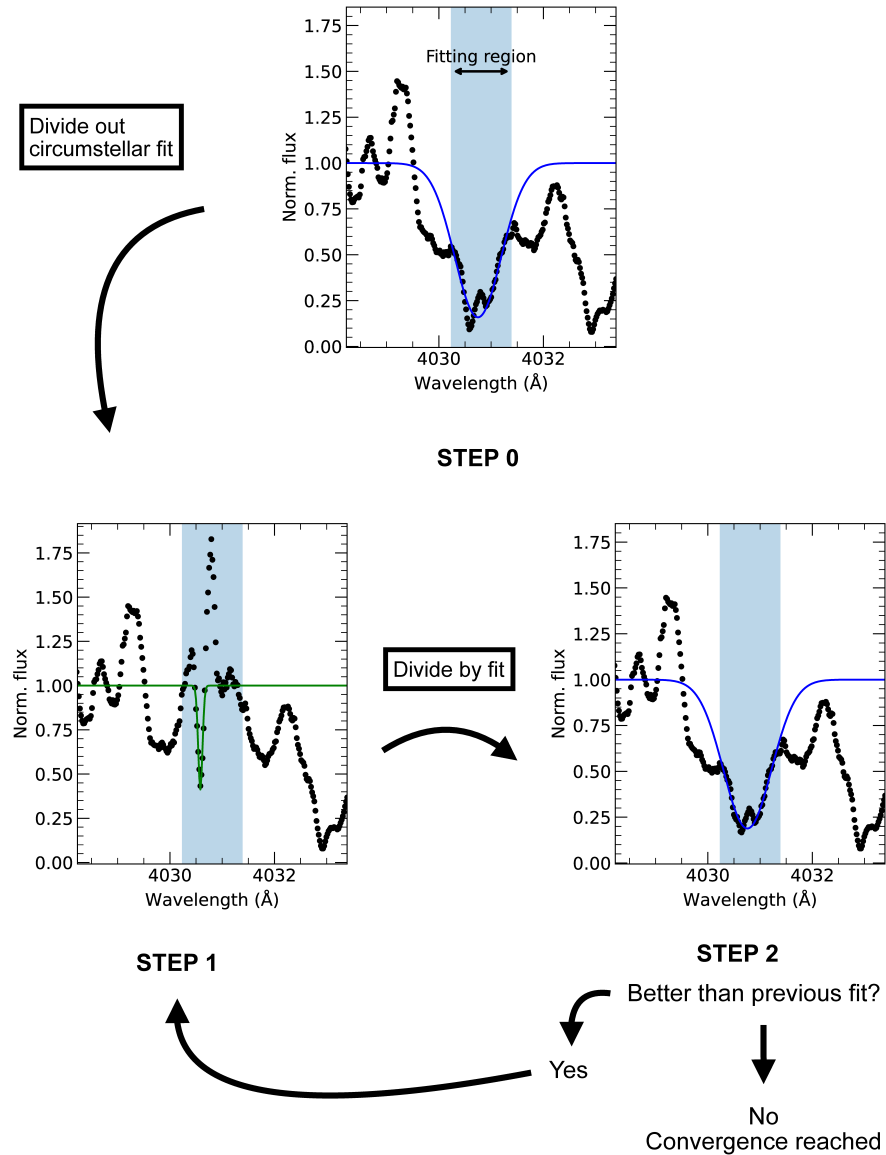


**Figure 6.** A HERMES spectrum of the Mn I transition at  $4030.75\text{\AA}$  illustrating the process of extracting the narrow circumstellar absorption profile. Step 0: a Gaussian profile (*blue line*) is fit to the broad photospheric absorption line. Step 1: A Gaussian profile is fit to the circumstellar profile (*green line*) after dividing by the photospheric Gaussian fit in Step 0. Step 2: The original line profile is divided by the fit to the circumstellar line (Step 1) to obtain the photospheric line profile, and a new Gaussian fit to the photospheric line is obtained (*blue line*). If this iteration improves the  $\chi^2$  between the model and the observed line, the process is repeated from Step 1 until no change occurs in the profile. Both the circumstellar line center and its EW are estimated from the Gaussian fit to the circumstellar line. The photospheric line center is taken from the Gaussian obtained in the final iteration.

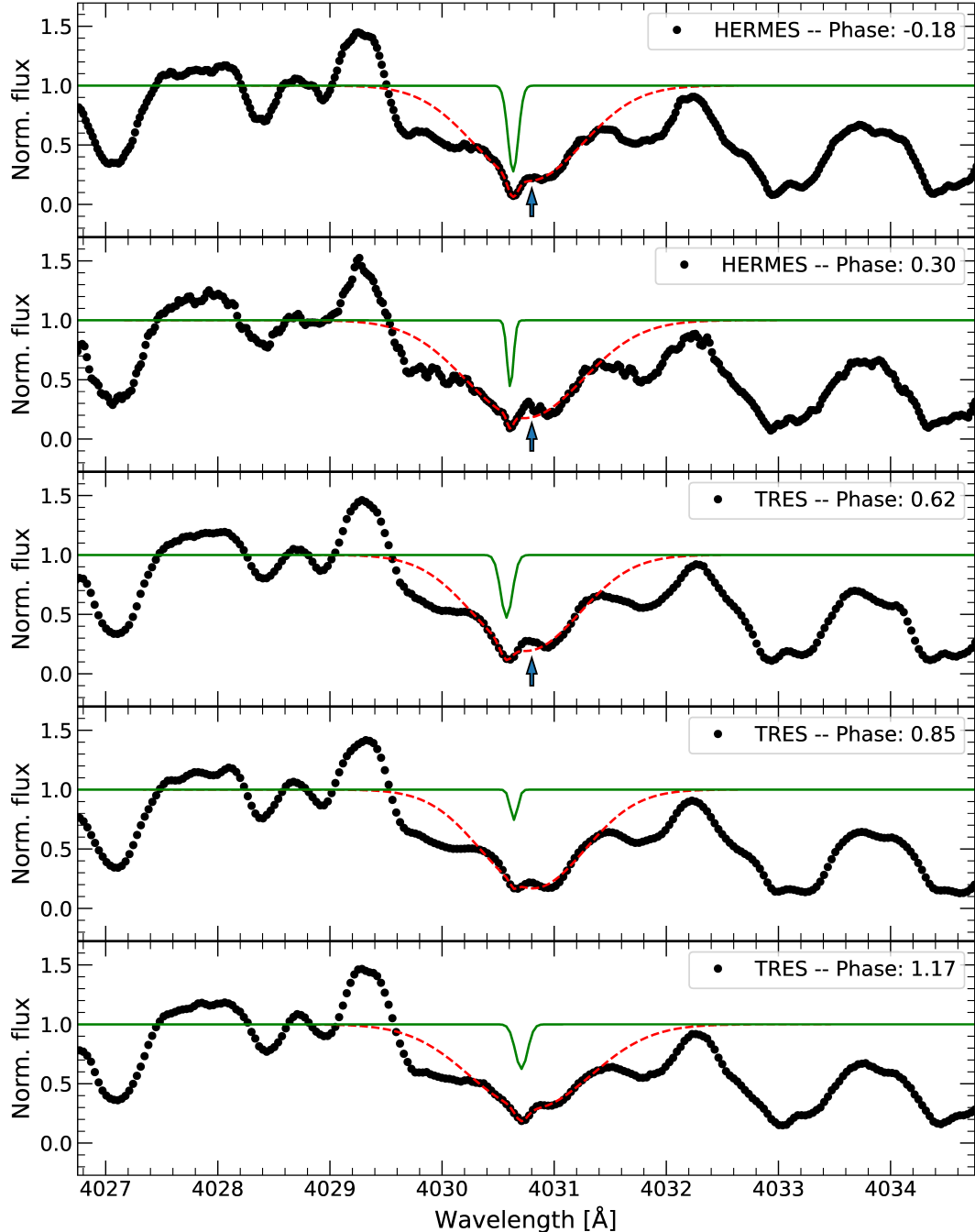


**Figure 7.** Sample spectra of the Mn I transition at 4030.75 Å from the HERMES and TRES observations. The narrow green line denotes the circumstellar absorption feature. The curve marked in red displays the fit to both features. Circumstellar emission can be seen in the core of the photospheric line and is marked by the upward arrow.

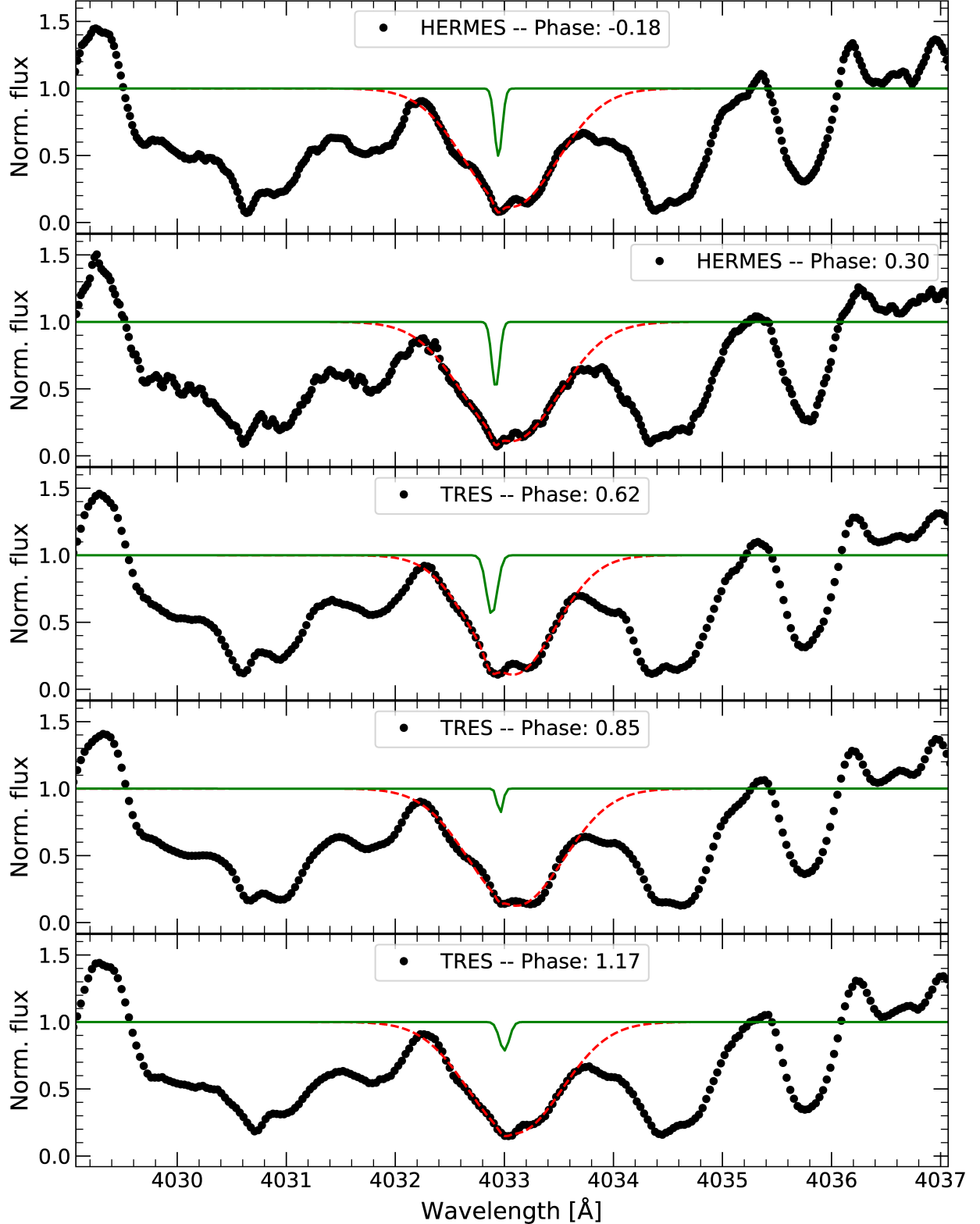


**Figure 8.** Spectra of the Mn I transition at  $4033.07\text{\AA}$  from HERMES and TRES observations. The curve marked in red displays the fit to the blended feature, and the narrow green line denotes the circumstellar absorption feature.

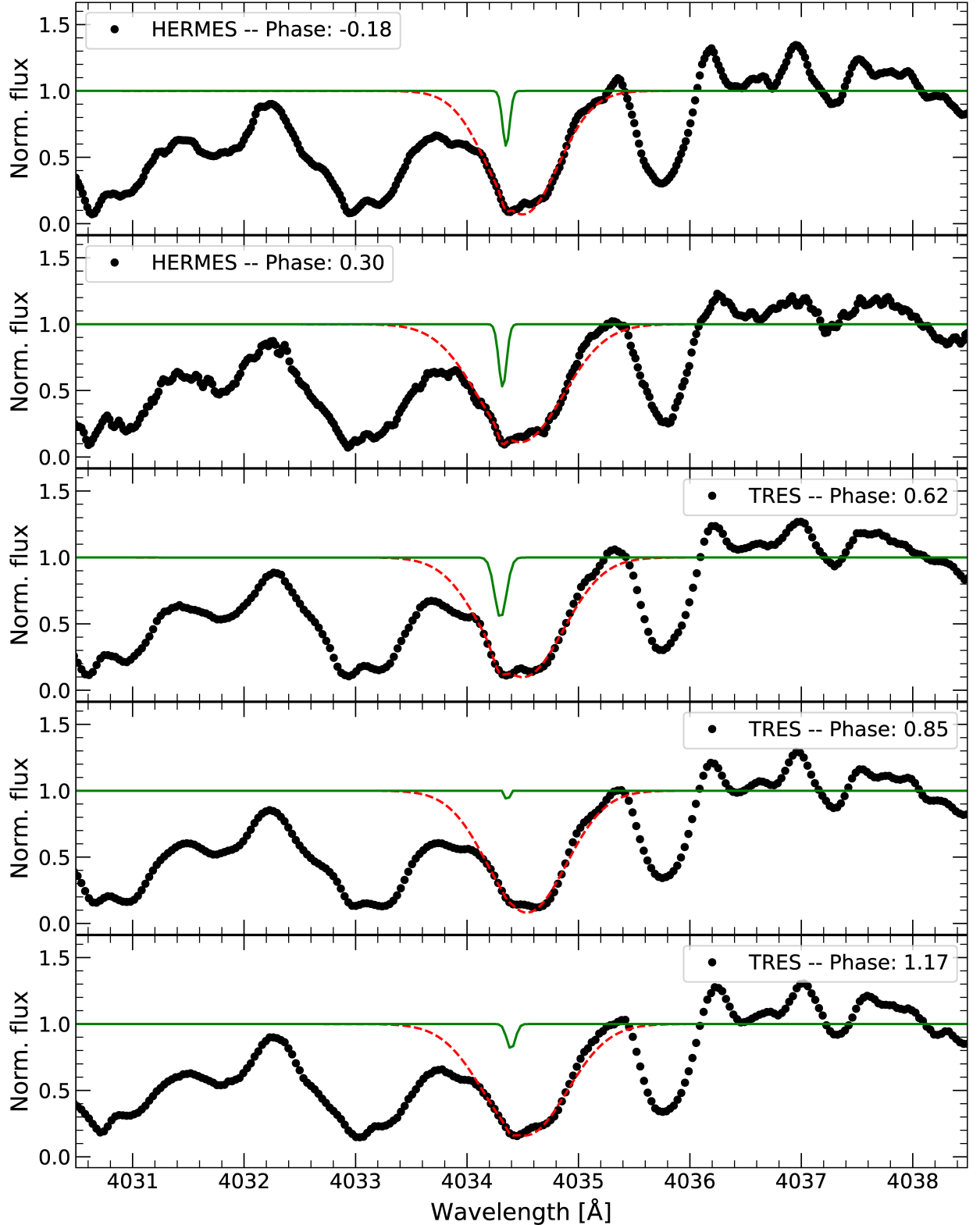


**Figure 9.** Spectra of the Mn I transition at  $4034.49\text{\AA}$  from HERMES and TRES observations. The curve marked in red displays the fit to the blended feature, and the narrow green line denotes the circumstellar absorption feature.

**Table 2.** STIS Spectra and Line Ratios

| Date       | JD        | Phase | STIS spectrum | Ratio Fe II | Ratio Mg I | Ratio Si I | Ratio Fe II | Ratio Fe II | Ratio Fe II | Ratio Fe II | 20 |
|------------|-----------|-------|---------------|-------------|------------|------------|-------------|-------------|-------------|-------------|----|
|            |           |       | 2692.8Å       | 2852.1Å     | 2516.1Å    | 2585.9Å    | 2724.8Å     | 2727.5Å     | 2730.7Å     |             |    |
| 2019-01-26 | 2458509.5 | 0.30  | odxg01040     | 0.56        | 1.47       | 0.95       | 0.95        | 1.06        | 0.81        | 0.99        |    |
| 2019-03-05 | 2458545.5 | 0.32  | odxg02040     | 0.55        | 1.50       | 0.88       | 0.99        | 1.21        | 0.82        | 1.01        |    |
| 2019-09-18 | 2458744.5 | 0.41  | odxg07040     | 0.48        | 1.47       | 0.97       | 1.06        | 1.16        | 0.96        | 1.16        |    |
| 2019-10-06 | 2458762.5 | 0.42  | odxg08040     | 0.51        | 1.45       | 1.05       | 1.02        | 1.14        | 0.90        | 1.15        |    |
| 2019-11-28 | 2458815.5 | 0.44  | oe1i01040     | 0.50        | 1.64       | 1.11       | 1.10        | 1.29        | 1.01        | 1.27        |    |
| 2020-02-03 | 2458882.5 | 0.48  | oe1i52040     | 0.40        | 1.52       | 1.09       | 1.00        | 0.93        | 0.65        | 0.81        |    |
| 2020-02-25 | 2458904.5 | 0.49  | oe1i103040    | 0.53        | 1.56       | 0.94       | 0.89        | 0.86        | 0.60        | 0.79        |    |
| 2020-04-02 | 2458941.5 | 0.50  | oe1i04040     | 0.45        | 1.49       | 0.84       | 0.86        | 1.02        | 0.60        | 0.78        |    |
| 2020-08-31 | 2459092.5 | 0.58  | oedq01040     | 0.51        | 1.27       | 0.90       | 1.06        | 0.97        | 0.71        | 0.89        |    |
| 2020-10-15 | 2459137.5 | 0.60  | oedq02040     | 0.42        | 1.18       | 0.92       | 0.93        | 0.88        | 0.60        | 0.79        |    |
| 2020-11-24 | 2459177.5 | 0.62  | oedq52040     | 0.40        | 1.13       | 0.75       | 0.95        | 0.95        | 0.63        | 0.76        |    |
| 2021-02-09 | 2459254.5 | 0.65  | oedq03040     | 0.47        | 1.12       | 0.82       | 0.95        | 1.25        | 0.75        | 0.96        |    |
| 2021-09-18 | 2459475.5 | 0.76  | oedq54040     | 0.71        | 1.44       | 1.19       | 1.37        | 1.84        | 1.08        | 1.41        |    |
| 2022-01-10 | 2459589.5 | 0.81  | oen702030     | 0.73        | 1.72       | 1.49       | 1.39        | 1.85        | 1.17        | 1.47        |    |
| 2022-02-10 | 2459620.5 | 0.83  | oen703030     | 0.87        | 1.75       | 1.32       | 1.22        | 1.85        | 1.14        | 1.44        |    |
| 2022-03-11 | 2459649.5 | 0.84  | oen704030     | 0.74        | 1.54       | 1.31       | 1.20        | 1.87        | 1.05        | 1.30        |    |
| 2022-04-11 | 2459680.5 | 0.85  | oen705030     | 0.85        | 1.60       | 1.33       | 1.33        | 2.00        | 1.18        | 1.43        |    |
| 2023-04-18 | 2460052.5 | 1.03  | oen751030     | 0.92        | 1.89       | 1.53       | 1.36        | 1.86        | 1.35        | 1.48        |    |
| 2023-09-27 | 2460214.5 | 1.11  | oevc01030     | 0.75        | 1.73       | 1.31       | 1.16        | 1.48        | 1.11        | 1.28        |    |
| 2023-11-13 | 2460261.5 | 1.13  | oevc02030     | 0.66        | 1.79       | 1.37       | 1.25        | 1.72        | 1.25        | 1.45        |    |
| 2024-02-13 | 2460353.5 | 1.17  | oevc03030     | 0.62        | 1.94       | 1.43       | 1.36        | 1.67        | 1.24        | 1.38        |    |
| 2024-03-23 | 2460392.5 | 1.19  | oevc04030     | 0.56        | 1.75       | 1.32       | 1.25        | 1.47        | 1.00        | 1.26        |    |
| 2024-09-27 | 2460580.5 | 1.28  | oevc05030     | 0.59        | 1.66       | 1.30       | 1.18        | 1.46        | 1.01        | 1.31        |    |
| 2024-11-17 | 2460631.5 | 1.31  | ofai01030     | 0.58        | 1.63       | 1.17       | 1.04        | 1.33        | 0.87        | 1.10        |    |
| 2024-12-20 | 2460668.5 | 1.32  | ofai02030     | 0.59        | 1.49       | 1.08       | 1.08        | 1.30        | 0.87        | 1.06        |    |
| 2025-08-27 | 2460914.5 | 1.44  | ofgk01040     | 0.56        | 1.44       | 1.00       | 1.17        | 1.27        | 0.91        | 1.12        |    |
| 2025-09-22 | 2460940.5 | 1.45  | ofgk02040     | 0.51        | 1.46       | 1.06       | 1.08        | 1.18        | 0.84        | 1.07        |    |
| 2025-10-17 | 2460965.5 | 1.46  | ofgk03040     | 0.48        | 1.43       | 1.00       | 1.06        | 1.06        | 0.81        | 0.98        |    |
| 2025-11-13 | 2460992.5 | 1.48  | ofgk04040     | 0.54        | 1.46       | 0.95       | 1.05        | 1.20        | 0.83        | 1.03        |    |